
Article:
Jones, M. orcid.org/0000-0003-2995-8303 and Clarke, N. orcid.org/0000-0002-1289-3016 (2025) Modeling the time evolution of the structure factor during polymeric spinodal decomposition using dynamic mode decomposition. The Journal of Chemical Physics, 163. 104904. ISSN: 0021-9606

https://doi.org/10.1063/5.0286708

The Journal of Chemical Physics

RESEARCH ARTICLE | SEPTEMBER 09 2025

Modeling the time evolution of the structure factor during polymeric spinodal decomposition using dynamic mode decomposition

Matthew Jones ; Nigel Clarke

J. Chem. Phys. 163, 104904 (2025)
https://doi.org/10.1063/5.0286708

The Journal of Chemical Physics ARTICLE pubs.aip.org/aip/jcp

Modeling the time evolution of the structure factor during polymeric spinodal decomposition using dynamic mode decomposition

Cite as: J. Chem. Phys. 163, 104904 (2025); doi: 10.1063/5.0286708
Submitted: 20 June 2025 • Accepted: 19 August 2025 •
Published Online: 9 September 2025

Matthew Jones[a] and Nigel Clarke[b]

AFFILIATIONS

School of Mathematical and Physical Sciences, University of Sheffield, Hicks Building, Hounsfield Road, Sheffield S3 7RH, United Kingdom

[a]matthew.hagley@blueyonder.co.uk. **Now at:** Infinitesima Limited.
[b]**Author to whom correspondence should be addressed:** n.clarke@sheffield.ac.uk

ABSTRACT

The development of the microstructure during polymeric spinodal decomposition can be monitored in real time using small-angle scattering. Information about the microstructure can be deduced from measurements of the structure factor—a quantity directly proportional to the scattered intensity. While the time evolution of the structure factor can be measured relatively easily, modeling it has proved to be much more difficult. We believe the latter could be impeding our ability to control spinodal decomposition. Using synthetic data corresponding to two different polymer blends, we investigate the use of dynamic mode decomposition to model the time evolution of the structure factor during polymeric spinodal decomposition. Based on the accuracy and range of the predictions we obtained using dynamic mode decomposition, we believe our results are promising for the use of dynamic mode decomposition in an experimental setting, which could improve our ability to control spinodal decomposition in automated experiments.

I. INTRODUCTION

Polymer blends, the polymer equivalent of metal alloys, offer the chance to develop new materials with unique properties. In general, polymer blends are prone to phase separation, leading to the formation of phase-separated microstructures, which affect the properties of the resulting material.[1] Phase separation can be key to the emergence of desirable properties—see, for example, Refs. 2–5.

In this paper, we are primarily concerned with thermally induced polymeric spinodal decomposition[6,7]—the process of spontaneous phase separation following a temperature change into the unstable region of the phase diagram. Depending on several factors, such as the temperature of the blend and the ratio of the constituent polymers, spinodal decomposition can give rise to a range of phase-separated microstructures, from dispersed droplets to co-continuous networks.[8,9] Polymeric materials with co-continuous microstructures have generated significant interest over recent years, finding applications in many industries, including renewable energy, membrane technology, and metamaterials.[2,4,5,10–12] Improving our ability to control spinodal decomposition could drive advances in these industries, as well as many others, by opening the door to the development of tailored, tunable microstructures.

The development of the microstructure during spinodal decomposition can be monitored in real time using small-angle scattering. Information about the microstructure can be deduced from measurements of the structure factor[13,14]—a quantity that is directly proportional to the scattered intensity. The equation of motion for the structure factor during spinodal decomposition is known to be unclosed.[15–17] In other words, it is an intractable infinite hierarchy of coupled differential equations. Existing attempts to model the time evolution of the structure factor have focused on deriving approximate equations of motion based on truncation schemes. One such approximate equation of motion is the linear Cahn–Hilliard–Cook–Flory–Huggins–de Gennes equation.[18–24] This equation has proved to be a useful tool in the analysis of

scattering data.[2,8,25–27] However, it is only applicable under a restrictive set of conditions and assumptions.[24,28,29] Motivated to improve this situation, Akcasu *et al.* set out to derive a non-linear equation of motion.[17,30,31] However, there is currently very little literature aimed at testing the Akcasu equation.[30] Consequently, we lack an adequate, verified model for the time evolution of the structure factor during spinodal decomposition. This impedes our ability to control the process: without an adequate model for the structure factor, it is not possible to make future predictions of the structure factor—valuable information for a control system. Predictions of the future evolution based on past and present data could be incorporated into a control system that uses the predictions to automatically adjust process parameters, such as temperature, in order to direct the phase separation toward a target structure with known properties. With this in mind, we propose the application of dynamic mode decomposition to the problem of modeling the time evolution of the structure factor. Dynamic mode decomposition is a quasi-linear and equation-free system identification technique for predicting the future, over a limited time window, based on past data. In this paper, we investigate the use of dynamic mode decomposition to predict future snapshots of the structure factor during spinodal decomposition based on the knowledge of previous snapshots. We work with synthetic time series of structure factor snapshots, which we generate ourselves. We assess the accuracy and range of the predictions obtained using dynamic mode decomposition, and we investigate the hyperparameter choices required to construct effective models.

II. THEORY

A. Polymeric spinodal decomposition

Let us consider an incompressible binary polymer blend. For simplicity, we assume equal degrees of polymerization, monomeric volumes, and Kuhn lengths.

Arguably, the most commonly used and successful theory for describing spinodal decomposition in polymer blends is the Cahn–Hilliard–Cook–Flory–Huggins–de Gennes (CHC-FHdG) theory.[18–24,32,33] Assuming a constant mobility,[24] M, and using the Flory–Huggins free energy supplemented with a non-local gradient term, the CHC-FHdG equation of motion takes the form

$$\frac{\partial\phi(\boldsymbol{r},t)}{\partial t} = \frac{Mk_BT}{v_0}\nabla^2\left[\frac{1}{N_A}\ln(\phi) - \frac{1}{N_B}\ln(1-\phi) - 2\chi\phi - \frac{\sigma^2}{18}\left(\frac{1}{\phi(1-\phi)}\right)\nabla^2\phi + \frac{\sigma^2}{36}\left(\frac{1-2\phi}{(\phi(1-\phi))^2}\right)(\nabla\phi)^2\right] + \xi(\boldsymbol{r},t), \tag{1}$$

where k_B is Boltzmann's constant, T is temperature, ϕ is the local volume fraction of polymer A, v_0 is the monomeric volume, χ is the interaction parameter, and σ is the Kuhn length. N_A and N_B are the degrees of polymerization of each polymer, which, for simplicity, we take to be equal for the remainder of our analysis, such that $N_A = N_B = N$. Again, for simplicity, we assume that both polymers have the same monomeric volumes and Kuhn lengths. The noise, $\xi(\boldsymbol{r},t)$, is assumed to be Gaussian distributed with the following moments:[15,20,29]

$$\langle\xi(\boldsymbol{r},t)\rangle = 0, \tag{2a}$$

$$\langle\xi(\boldsymbol{r},t)\xi(\boldsymbol{r}',t')\rangle = B\delta(\boldsymbol{r}-\boldsymbol{r}')\delta(t-t'), \tag{2b}$$

where B is an operator—the form of which ensures any change in $\phi(\boldsymbol{r},t)$ due to $\xi(\boldsymbol{r},t)$ is balanced by the correct flux. In other words, B ensures no material is created or destroyed. To determine B, it is assumed that the system will evolve to its equilibrium state over a sufficiently long time period. Non-linear Langevin equations, such as Eq. (1), are hard to solve analytically. The most practical approach to deal with them is to construct the corresponding Fokker–Planck equation, which describes the time evolution of the probability distribution of the order parameter,[34,35]

$$\frac{\partial P(\{\phi(\boldsymbol{r})\},t)}{\partial t} = \int d^3r\frac{\delta}{\delta\phi}\left[-M\nabla^2\frac{\delta F}{\delta\phi}P + \frac{B}{2}\frac{\delta P}{\delta\phi}\right]. \tag{3}$$

As $t\to\infty$, the solution to Eq. (1) approaches the equilibrium solution. Equilibrium thermodynamics tells us this should be a Boltzmann distribution; therefore,[34]

$$B = -2Mk_BT\nabla^2. \tag{4}$$

Specifically, it is the factor of ∇^2 in B that ensures material is conserved. We discuss this point further in Sec. S.1.1 of the supplementary material.

In its current form, Eq. (1) can only be solved numerically. To make it analytically tractable, we must linearize it.[23,24] Upon making the substitution $\phi(\boldsymbol{r},t) = \phi_0 + \delta\phi(\boldsymbol{r},t)$, where ϕ_0 is the average volume fraction and $\delta\phi$ is a fluctuation, performing a power series expansion, and neglecting all non-linear terms in $\delta\phi(\boldsymbol{r},t)$, we obtain

$$\frac{\partial\delta\phi(\boldsymbol{r},t)}{\partial t} = \frac{Mk_BT}{v_0}\left[2(\chi_s-\chi)\nabla^2\delta\phi - \frac{\sigma^2}{18}\left(\frac{1}{\phi_0(1-\phi_0)}\right)\nabla^4\delta\phi\right] + \xi(\boldsymbol{r},t), \tag{5}$$

where $\chi_s = 2/4N\phi_0(1-\phi_0)$ is the value of the interaction parameter on the spinodal. We refer to Eq. (5) as the linear CHC-FHdG equation. In the case of spinodal decomposition, we expect the linear CHC-FHdG equation to be valid during the early stage, i.e., when the composition fluctuations are small.[28,32] Upon comparing Eq. (5) with Fick's second law, we can identify the mutual diffusion coefficient of the blend as[2]

$$D = \frac{2Mk_BT(\chi_s-\chi)}{v_0}. \tag{6}$$

In the case of spinodal decomposition, D is negative. Therefore, diffusion occurs against the composition gradient, or "uphill," which leads to phase separation. The solution to Eq. (5) without noise is given by[32]

$$\delta\phi(\boldsymbol{r},t) = \sum_{\boldsymbol{q}}\exp(R(q)t)(A(\boldsymbol{q})\cos(\boldsymbol{q}\cdot\boldsymbol{r}) + B(\boldsymbol{q})\sin(\boldsymbol{q}\cdot\boldsymbol{r})), \tag{7}$$

where A and B are the initial amplitudes of the composition fluctuations present in the sample, and

$$R(q) = -\frac{Mk_BT}{v_0}\left[2(\chi_s-\chi)q^2 + \frac{\sigma^2}{18}\left(\frac{1}{\phi_0(1-\phi_0)}\right)q^4\right], \tag{8}$$

is a q-dependent amplification factor. The symbol q denotes the wavenumber of a composition fluctuation, which is related to the

wavelength via $\lambda = 2\pi/q$. By calculating the value of q that corresponds to the maximum value of R, one can predict the wavelength of the fastest-growing composition fluctuations, which defines the characteristic length scale of the blend during the early stage of spinodal decomposition.

The linear CHC-FHdG equation has been shown to quantitatively capture the early stage of spinodal decomposition in polymer blends.[2,25,26,29] Beyond the early stage, the non-linear CHC-FHdG equation qualitatively captures the dynamics of the process.[32,36] For example, it captures coarsening and can be used to generate simulated morphologies that are representative of spinodal decomposition.

B. Small-angle scattering

Small-angle scattering experiments are often used to monitor the time evolution of composition fluctuations, i.e., the development of the microstructure in polymer blends.[2,13,14,27] The intensity of the scattered radiation is directly proportional to a quantity called the structure factor. One can learn about the microstructure by analyzing the structure factor.[2,13,14,37] For example, in the case of spinodal decomposition, the characteristic length can be determined from the peak. The structure factor is essentially the power spectrum of the composition fluctuations, i.e., the product of the Fourier transform with its complex conjugate. It is not possible to obtain full knowledge of the microstructure from the structure factor.[14] The structure factor can be written compactly as[14]

$$S(q,t) = \frac{1}{V}\langle P(q,t)\rangle, \tag{9}$$

where $P(q,t)$ is the power spectrum of $\phi(\boldsymbol{r})$,

$$P(q,t) = \delta\phi(q,t)\delta\phi(-q,t), \tag{10}$$

where V is the volume of the system, $\langle\cdots\rangle$ denotes a time average, and $\delta\phi(q) = \int d^3r\delta\phi(\boldsymbol{r})\exp(-i\boldsymbol{q}\cdot\boldsymbol{r})$, i.e., $\delta\phi(q)$ is the Fourier transform of $\phi(\boldsymbol{r})$. In isotropic systems, the structure factor depends on q instead of $\boldsymbol{q}$. In the absence of external fields, we expect phase separation in polymer blends to be isotropic. In an experimental context, $S(q,t)$ is calculated as the radial average of a two-dimensional scattering image, $S(\boldsymbol{q},t)$.[13,36]

Differentiating Eq. (9) with respect to time, we obtain the following equation of motion for the structure factor in terms of $\partial\delta\phi(q,t)/\partial t$,

$$\frac{\partial S(q,t)}{\partial t} = \frac{1}{V}\left\langle\frac{\partial\delta\phi(q)}{\partial t}\delta\phi(-q)\right\rangle + \frac{1}{V}\left\langle\delta\phi(q)\frac{\partial\delta\phi(-q)}{\partial t}\right\rangle. \tag{11}$$

Using the CHC-FHdG equation for the equation of motion for $\delta\phi(q,t)$, i.e., $\partial\delta\phi(q,t)/\partial t$, we obtain the following linearized equation of motion:

$$\frac{\partial S(q,t)}{\partial t} = 2R(q)S(q,t) + 2Mk_BTq^2. \tag{12}$$

The amplification factor can be written as[38]

$$R(q) = -Mk_BTq^2S_T^{-1}(q), \tag{13}$$

where S_T is the stationary solution to Eq. (12),

$$S_T(q) = v_0\left[2(\chi_s - \chi) + \frac{\sigma^2}{18}\left(\frac{1}{\phi_0(1-\phi_0)}\right)q^2\right]^{-1}. \tag{14}$$

In dissolution, S_T coincides with the small-q limit of de Gennes' random phase approximation for the static structure factor.[38,39] In spinodal decomposition, S_T coincides with the small-q limit of the "virtual" structure factor.[38,39] The solution to Eq. (12) is given by[38]

$$S(q,t) = (S(q,0) - S_T)\exp(2R(q)t) + S_T(q). \tag{15}$$

From this solution, a fitting relationship can be established to calculate $R(q)$ from experimental (or simulated) data.[2] This provides a means of testing the linear CHC-FHdG equation, which, as we mentioned earlier, has been shown to quantitatively capture the early stage of spinodal decomposition in polymer blends.

The linear CHC-FHdG equation for the structure factor [Eq. (12)] is only valid during the early stage of spinodal decomposition, i.e., while composition fluctuations are small. Therefore, the validity of the linear CHC-FHdG equation is limited. Motivated to improve this situation, Akcasu *et al.* set out to develop an approximate, tractable, non-linear equation of motion for the structure factor.[17,30,31] Their equation is based on that of Langer *et al.*,[40] who worked on the same problem but in the context of small molecule mixtures.

The derivation of the Akcasu equation is quite long. Therefore, we simply quote the result in its simplest, most interpretable form

$$\frac{\partial S(q,t)}{\partial t} = 2R(q)S(q,t)[1 + Z(q,t)] - 2R(q)S_{\mathrm{eq}}(q)[1 + Z_{\mathrm{eq}}(q)], \tag{16}$$

where $Z(q,t)$ is a non-linear mode-coupling term, $Z_{\mathrm{eq}}(q)$ is the equilibrium value of $Z(q,t)$, and $S_{\mathrm{eq}}(q)$ is the equilibrium value of $S(q,t)$. The mode-coupling term describes the coupling of composition fluctuations with different wavelengths. The term after the minus sign on the right-hand side is the noise term, which ensures the correct long-time (equilibrium) behavior of $S(q,t)$. As a result of the closure approximations introduced by Akcasu *et al.*, the noise term here is, in general, different from that in Eq. (12).

There has been no reported comparison between the predictions of the Akcasu equation and numerical or experimental measurements of the structure factor in the case of spinodal decomposition. In the case of dissolution, a comparison with experimental data was performed by Akcasu *et al.*[30] The comparison revealed a quantitative discrepancy between theory and experiment, which worsened as the dissolution time increased. Akcasu *et al.* used best-guess values of molecular and thermodynamic parameters to solve their equation because some of the parameters are hard to measure. It is unclear whether the Akcasu equation failed as a result of the equation being inadequate or incorrect parameter values being used. It is this uncertainty and lack of a tested model that result in the duality that, although it is relatively easy to measure, it is much harder to model the structure factor.[15,16] As a consequence, there is no reliable methodology for quantitatively predicting the evolution based on real-time measurements. This duality motivates our work described below, in which we show that a data driven approach to predicting the evolution of the structure factor is a viable alternative to physics based modeling.

C. Dynamic mode decomposition

Dynamical systems are ubiquitous in a wide range of fields. In many of these fields, there is a duality between abundant measurement data and elusive governing equations,[41] i.e., differential equations describing a process of interest. Embracing this duality, the field of system identification, concerned with building models of dynamical systems from measurement data, has emerged as an alternative to traditional theory-driven modeling.[41]

In this paper, we consider a linear system identification technique called dynamic mode decomposition (DMD). Developed by Schmid[42] in the field of fluid mechanics before being developed by others,[41,43,44] DMD is an algorithm for calculating the leading eigenvectors and eigenvalues of the best-fit linear operator $\mathbf{A}$ that approximately describes the dynamics of a high-dimensional, non-linear, spatio-temporal system. A purely data-driven technique, DMD only requires snapshots of the system as an input. Examples of applying DMD and its extensions, including code, can be found in Ref. 45. We outline DMD below.[41,44]

DMD is formulated based on the following equation:

$$\mathbf{X}' \approx \mathbf{A}\mathbf{X}, \tag{17}$$

where $\mathbf{X}$ and $\mathbf{X}'$ are data matrices comprised of snapshots $\mathbf{x}_k$ appended column-wise. Given m snapshots sampled every Δt in time, the data matrices are given by

$$\mathbf{X} = \begin{bmatrix} | & | & | & | \\ \mathbf{x}_1 & \mathbf{x}_2 & \dots & \mathbf{x}_{m-1} \\ | & | & | & | \end{bmatrix}, \tag{18}$$

and

$$\mathbf{X}' = \begin{bmatrix} | & | & | & | \\ \mathbf{x}_2 & \mathbf{x}_3 & \dots & \mathbf{x}_{m} \\ | & | & | & | \end{bmatrix}. \tag{19}$$

One might wonder about the point of using DMD to calculate the eigendecomposition of $\mathbf{A}$ when they could calculate $\mathbf{A}$ directly using least-squares regression instead,

$$\mathbf{A} = \arg\min_{\mathbf{A}} \|\mathbf{X}' - \mathbf{A}\mathbf{X}\|_F = \mathbf{X}'\mathbf{X}^{\dagger}, \tag{20}$$

where F denotes the Frobenius norm and † denotes the Moore–Penrose pseudoinverse.[46] The motivation for the approach adopted in DMD is that the calculation in Eq. (20) can prove problematic if $\mathbf{A}$ is high-dimensional. Given that each snapshot contains n elements, $\mathbf{A}$ will contain n^2 elements. Therefore, if n is large, just representing $\mathbf{A}$ could be problematic, let alone performing calculations involving it.

To circumvent any calculations that directly involve $\mathbf{A}$, DMD makes use of dimensionality reduction through singular value decomposition (SVD),[41] a data-driven technique for matrix factorization. The SVD factorization is structured in such a way that a low-dimensional, or low-rank, approximation to the original matrix is often easy to obtain. To illustrate this, we consider the SVD of $\mathbf{X}$. Given that the snapshots $\mathbf{x}_k$ contain n elements, meaning $\mathbf{X} \in \mathbb{R}^{n\times(m-1)}$, the SVD of $\mathbf{X}$ is given by

$$\mathbf{X} = \mathbf{U}\mathbf{\Sigma}\mathbf{V}^{*}, \tag{21}$$

where $\mathbf{U} \in \mathbb{R}^{n\times n}$ and $\mathbf{V} \in \mathbb{R}^{(m-1)\times(m-1)}$ are unitary matrices with orthonormal columns and $\mathbf{\Sigma} \in \mathbb{R}^{n\times(m-1)}$ is a diagonal matrix with real, positive entries, collectively referred to as singular values. The symbol * denotes the complex conjugate transpose. The columns of $\mathbf{U}$ are referred to as proper orthogonal decomposition (POD) modes. These modes are a superposition of patterns or signals in the data. When POD modes are constructed, temporal information is largely ignored—typically, patterns or signals that oscillate at different frequencies are mixed. The rows of $\mathbf{V}^{*}$ describe the time evolution of the POD modes. The singular values in $\mathbf{\Sigma}$ are ordered hierarchically. The magnitude of a given singular value ranks the relative importance of the corresponding POD mode in $\mathbf{U}$ for describing the data in $\mathbf{X}$, i.e., the first POD mode is more important than the second, and so on. Therefore, to calculate a low-rank approximation to $\mathbf{X}$, one can simply choose to keep the leading $\tilde{r}$ columns of $\mathbf{U}$, rows of $\mathbf{V}^{*}$, and singular values in $\mathbf{\Sigma}$, discarding everything else,

$$\mathbf{X} \approx \tilde{\mathbf{U}}\tilde{\mathbf{\Sigma}}\tilde{\mathbf{V}}^{*}, \tag{22}$$

where $\tilde{\mathbf{U}} \in \mathbb{C}^{n\times\tilde{r}}$, $\tilde{\mathbf{V}} \in \mathbb{C}^{(m-1)\times\tilde{r}}$, $\tilde{\mathbf{\Sigma}} \in \mathbb{R}^{\tilde{r}\times\tilde{r}}$, and $\tilde{r} < m-1$. Choosing the rank $\tilde{r}$ is an important, albeit often subjective, part of this dimensionality reduction procedure. A heuristic approach is to locate "elbows" in an ordered plot of the singular values. The resulting reduced SVD defines a low-dimensional, orthogonal coordinate system in which the data in $\mathbf{X}$ can be represented. Functions for calculating the SVD are standard in most programming languages. References regarding the numerical implementation of the SVD can be found in Ref. 41.

We are now in a position to outline the DMD algorithm. The first step is to calculate the reduced SVD of the data matrix $\mathbf{X}$, which is given by Eq. (22). The second step is to project $\mathbf{A}$ onto the POD modes in $\tilde{\mathbf{U}}$,

$$\tilde{\mathbf{A}} = \tilde{\mathbf{U}}^{*}\mathbf{A}\tilde{\mathbf{U}} = \tilde{\mathbf{U}}^{*}\mathbf{X}'\tilde{\mathbf{V}}\tilde{\mathbf{\Sigma}}^{-1}. \tag{23}$$

The reduced matrix $\tilde{\mathbf{A}}$ has the same nonzero eigenvalues as the full matrix $\mathbf{A}$. It is this step that enables one to circumvent calculations that directly involve $\mathbf{A}$. The third step is to calculate the eigendecomposition of $\tilde{\mathbf{A}}$,

$$\tilde{\mathbf{A}}\mathbf{W} = \mathbf{W}\mathbf{\Lambda}, \tag{24}$$

where $\mathbf{W}$ contains the eigenvectors of $\tilde{\mathbf{A}}$, appended column-wise, and $\mathbf{\Lambda}$ is a diagonal matrix containing the eigenvalues. The final step, developed by Tu *et al.*,[41,43] is to construct the eigenmodes of $\mathbf{A}$ from $\mathbf{W}$,

$$\mathbf{\Phi} = \mathbf{X}'\tilde{\mathbf{V}}\tilde{\mathbf{\Sigma}}^{-1}\mathbf{W}. \tag{25}$$

We subsequently refer to these modes as DMD modes.

With knowledge of $\mathbf{\Phi}$ and $\mathbf{\Lambda}$, one can use the following equation to reconstruct the data in $\mathbf{X}$ and make predictions of future snapshots:[41]

$$\mathbf{x}_k \approx \mathbf{\Phi}\,\exp(\mathbf{\Omega}k\Delta t)\boldsymbol{b}, \tag{26}$$

where $\mathbf{\Omega} = \ln(\mathbf{\Lambda})/\Delta t$ and $\boldsymbol{b}$ is a vector of coefficients. The vector $\boldsymbol{b}$ can be calculated in two ways: either directly using $\boldsymbol{b} = \mathbf{\Phi}^{\dagger}\mathbf{x}_1$ or indirectly using a projection onto the POD modes. In contrast to POD modes, DMD modes consist of patterns or signals in the data that oscillate, with growth or decay, at the same frequency. The

oscillatory behavior is described by the corresponding eigenvalue. In general, the eigenvalues are complex. The real part encapsulates growth or decay, while the imaginary part encapsulates periodic behavior. Eigenvalues with a modulus greater than or equal to one are unstable, limiting how far one can use Eq. (26) to accurately and reliably predict into the future.

To summarize the application of the DMD methodology to our work, synthetic snapshots of the structure factor are used to construct the matrices $\mathbf{X}$ and $\mathbf{X}'$ [Eqs. (18) and (19)]. Each column in the two matrices represents one snapshot in time of the structure factor, with each row representing the value of the structure factor at a given value of q. As indicated in Eqs. (18) and (19), only the first column of $\mathbf{X}$ and the last column of $\mathbf{X}'$ are unique between the two matrices. Rather than directly calculating the matrix $\mathbf{A}$ of Eq. (17), we then numerically undertake the four steps outlined in Eqs. (22)–(24). We are then able to make predictions of future iterations of the structure factor using Eq. (26).

III. METHODOLOGY

A. Generating time series of synthetic structure factor snapshots

1. Overview and key equations

We used two time series of synthetic structure factor snapshots to obtain the results in Sec. IV. An overview of the method we used to generate each time series is as follows:

- We simulated polymeric spinodal decomposition using a finite difference scheme, namely a non-dimensionalized and discretized version of the CHC-FHdG equation [Eq. (1)].
- During the simulations, we calculated snapshots of the power spectrum using a modified version of Eq. (10).
- After running several repeat simulations, we calculated snapshots of the structure factor by applying a modified version of Eq. (9) to the power spectrum snapshots we accumulated.

There are three key equations: the finite difference scheme and the equations we used to calculate the snapshots of the power spectrum and the structure factor. We present these equations below. In the interest of orderliness, we defer the derivations of the equations to Sec. S.1.1 of the supplementary material.

a. Finite difference equation. To simulate polymeric spinodal decomposition, we applied the following finite difference scheme—a non-dimensionalized and discretized version of Eq. (1)—to a simple cubic lattice with periodic boundary conditions,

$$\begin{aligned}\phi^{m+1}_{j,k,l} = \phi^{m}_{j,k,l} + \frac{\Delta\tau}{2\Delta x^2}\sum_{nn}\left[\frac{\chi_c}{2|\chi-\chi_s|}\ln\left(\frac{\phi^m_{j,k,l}}{1-\phi^m_{j,k,l}}\right) - \frac{2\chi\phi^m_{j,k,l}}{|\chi-\chi_s|}\right.\\ + \frac{1}{36}\left(\frac{1-2\phi^m_{j,k,l}}{(\phi^m_{j,k,l}(1-\phi^m_{j,k,l}))^2}\right)\frac{1}{4\Delta x^2}\prod_{nn}\phi^m_{j,k,l}\\ \left. - 2\left(\frac{1}{36\phi^m_{j,k,l}(1-\phi^m_{j,k,l})}\right)\frac{1}{\Delta x^2}\sum_{nn}\phi^m_{j,k,l}\right] + \frac{v_0^{1/2}|\chi-\chi_s|^{1/4}}{\sigma^{3/2}}\\ \times\frac{1}{\Delta x}\left[\eta^m_{1;j+1,k,l} - \eta^m_{1;j,k,l} + \eta^m_{2;j,k+1,l} - \eta^m_{2;j,k,l} + \eta^m_{3;j,k,l+1} - \eta^m_{3;j,k,l}\right],\end{aligned} \tag{27}$$

where m denotes the number of dimensionless time steps, $\Delta\tau$ is the duration of a dimensionless time step, j, k, and l denote the coordinates of each lattice site, Δx is the dimensionless length of each lattice site, $\sum_{nn}$ and $\prod_{nn}$ are short-hand operators, and η_1, η_2, and η_3 are dimensionless Gaussian random variables. The shorthand operators are defined as

$$\sum_{nn} f_{j,k,l} = f_{j+1,k,l} + f_{j-1,k,l} + f_{j,k+1,l} + f_{j,k-1,l} + f_{j,k,l+1} + f_{j,k,l-1} - 6f_{j,k,l}, \tag{28a}$$

$$\begin{aligned}\prod_{nn} f_{j,k,l} = f^2_{j+1,k,l} + f^2_{j-1,k,l} + f^2_{j,k+1,l} + f^2_{j,k-1,l} + f^2_{j,k,l+1} + f^2_{j,k,l-1}\\ - 2(f_{j+1,k,l}f_{j-1,k,l} + f_{j,k+1,l}f_{j,k-1,l} + f_{j,k,l+1}f_{j,k,l-1}).\end{aligned} \tag{28b}$$

The first and second moments of the Gaussian random variables are given by

$$\left\langle \eta^m_{n;j,k,l}\right\rangle = 0, \tag{29a}$$

$$\left\langle \eta^m_{n;j,k,l}\eta^{m'}_{n';j',k',l'}\right\rangle = \frac{\Delta\tau}{\Delta x^3}\delta_{n,n'}\delta_{j,j'}\delta_{k,k'}\delta_{l,l'}\delta_{m,m'}. \tag{29b}$$

The dimensionless variables we used to obtain Eq. (27) are as follows:

$$\boldsymbol{x} = \frac{|\chi-\chi_s|^{1/2}}{\sigma}\,\boldsymbol{r}, \tag{30a}$$

$$\tau = \frac{2Mk_BT|\chi-\chi_s|^2}{\sigma^2 v_0}\,t, \tag{30b}$$

$$\tilde{\xi}(\boldsymbol{x},\tau) = \frac{\sigma^2 v_0}{2Mk_BT|\chi-\chi_s|^2}\,\xi(\boldsymbol{r},t). \tag{30c}$$

These dimensionless variables are inspired by those in Ref. 36. They relate to the fastest growing wavelength and its growth rate during the early stage of spinodal decomposition.

In the context of lattice sites in the top row of a cubic lattice, periodic boundary conditions mean that the nearest neighbors in the vertical direction are the corresponding lattice sites in the bottom row. The nearest neighbors to the left of lattice sites in the left-most row, to the right of lattice sites in the right-most row, and below lattice sites in the bottom row follow analogously.

For later reference, we denote the total number of time steps in a simulation as $m_{\max}$.

b. Snapshots of the power spectrum. To calculate snapshots of the power spectrum during the simulations, we used

$$\begin{aligned}\tilde{P}^m_{n;d} = \Delta x^6\left\langle\sum_{j=0}^{N_s-1}\sum_{k=0}^{N_s-1}\sum_{l=0}^{N_s-1}\delta\phi^m_{n;j,k,l}\,e^{-\frac{2\pi i}{N_s}(aj+bk)}\right.\\ \left.\times\sum_{j'=0}^{N_s-1}\sum_{k'=0}^{N_s-1}\sum_{l'=0}^{N_s-1}\delta\phi^{m'}_{n;j',k',l'}e^{\frac{2\pi i}{N_s}(aj'+bk')}\right\rangle_R,\end{aligned} \tag{31}$$

where n allows one to distinguish between repeat simulations, N_s is the number of lattice sites in each dimension of the cubic simulation lattice, a and b are integers in the range $-(N_s-1)/2 \le a, b \le (N_s-1)/2$, and $\langle\cdots\rangle_R$ denotes a radial average. Note that

Eq. (31) represents the sum along one dimension of a series of two-dimensional Fourier transforms. We have chosen this method to calculate the power spectrum, as it most closely conforms to a small angle experiment in which the magnitude of the scattering vector parallel to the incoming beam is negligible compared to the magnitude of the scattering vector perpendicular to the beam (i.e., in the plane of the detector). This is quantified further in the supplementary material. The radial average can be written explicitly as

$$\langle f_{a,b}\rangle_R \equiv f_d = \frac{\sum_{a,b \text{ s.t. round}(\sqrt{a^2+b^2})=d} f_{a,b}}{\sum_{a,b \text{ s.t. round}(\sqrt{a^2+b^2})=d} 1}, \tag{32}$$

where d is an integer in the range $0 \le d \le \frac{N_s-1}{2}$.

c. Snapshots of the structure factor. After implementing N_r repeat simulations, we calculated snapshots of the structure factor using

$$\tilde{S}_d^m = \frac{1}{N_r N_s^3 \Delta x^3} \sum_{n=1}^{N_r} \tilde{P}_{n;d}^m. \tag{33}$$

Throughout the remainder of the paper, we express snapshots of $\tilde{S}_d^m$ as $\tilde{S}(\mathrm{k},\tau)$, where $\mathrm{k} = 2\pi d/N_s\Delta x$ and $\tau = m\Delta\tau$. The symbol k denotes the magnitude of the dimensionless scattering vector, i.e., $\mathrm{k} = |\mathbf{k}|$.

We note that Eqs. (31) and (33) are non-dimensional and discrete, consistent with Eq. (27). The non-dimensionalization was performed using Eq. (30a) and the dimensionless variables below:

$$\mathrm{k} = \frac{\sigma}{|\chi-\chi_s|^{\frac{1}{2}}} q, \tag{34a}$$

$$\tilde{S}(\mathrm{k},\tau) = \frac{|\chi-\chi_s|^{\frac{3}{2}}}{\sigma^3} S(q,t). \tag{34b}$$

2. Parameter values and initial conditions

Each of the time series we generated corresponds to a different combination of ϕ_0 and χ values. For ease of reference, we devised a name for each time series based on these values (see Table I). We implemented five repeat simulations ($N_r = 5$) for each combination of ϕ_0 and χ values. In each simulation, we set the initial composition at each lattice site equal to the corresponding value of ϕ_0. After the first time step, the Gaussian random variable term in Eq. (27) introduced random fluctuations into the composition, initiating spinodal decomposition. We calculated snapshots of the power spectrum after the first and every 400th time step, i.e., when $m = 1, 400, 800, 1200$, etc. The values of the other parameters we used in the simulations were $\Delta x = 0.25$, $\Delta\tau = 6.25 \times 10^{-5}$, $N_s = 257$, $m_{\max} = 8 \times 10^5$, $N = 2700$, and $\sigma = \sqrt{20} v_0^{\frac{1}{3}}$, where the factor of $\sqrt{20}$ is the square root of the characteristic ratio, $C_\infty = \sigma^2/v_0^{\frac{2}{3}}$. In the case of the critical time series, the value of χ_s corresponding to $N = 2700$ is $\chi_s = 0.000\,741$, while in the case of the off-critical time series, it is $\chi_s = 0.000\,814$. We based the values of N and χ on those used in Refs. 47–49. The value of C_∞ corresponds to a relatively stiff polymer.[50] We found using larger values of C_∞ increased the numerical stability of the simulations, which we believe is due to a resultant reduction in the magnitude of the noise term in Eq. (27). Large values of noise will cause large gradients in the composition, which can lead to overshoot errors in the finite difference approximation to the equation of motion unless much smaller, computationally prohibitive, values of Δx and $\Delta\tau$ are used. We used trial and error to determine suitable values of Δx and $\Delta\tau$, i.e., values of Δx and $\Delta\tau$ that can be used in the simulations to generate time series that are independent of these values. Further details on this are provided in Sec. S.1.2 of the supplementary material.

TABLE I. Values of ϕ_0 and χ corresponding to each time series we generated.

Time series name	ϕ_0	χ
Critical (spinodal decomposition)	0.5	0.000 765
Off-critical (spinodal decomposition)	0.35	0.000 937

3. Implementing the simulations

We implemented the simulations in Julia.[51] To keep the computation time to a minimum, we made use of the CUDA.jl package.[52] This allowed us to implement Eq. (27) on a graphics processing unit (GPU), which we accessed on the University of Sheffield's high-performance computer, Stanage. The code we developed to implement the simulations is available on ORDA, the University of Sheffield's research data repository. Text files from which the time series can be calculated using Eq. (33) are also located there. Please see the Data Availability statement at the end of the paper for more details.

4. Conforming with the small-k limit

As we have already mentioned, Eq. (27) is a non-dimensionalized and discretized version of Eq. (1). Since Eq. (1) is only valid in the small-q limit, it follows that Eq. (27) is only valid in the corresponding small-k limit. The small-k limit is somewhat ambiguously defined as $\mathrm{k}r_g \ll 1$, where r_g is the dimensionless radius of gyration. To determine whether to truncate the snapshots of the synthetic structure factor we generated to conform with the small-k limit when obtaining our results, we attempted to quantify the small-k limit.

We determined inequalities that specify the small-k limit corresponding to each time series. We then compared these inequalities with the k-values associated with the constituent snapshots. In the case of the critical-time series, we determined the small-k limit corresponds to $\mathrm{k} < 5$, and in the case of the off-critical time series, we determined $\mathrm{k} < 3$. In the derivation of the random phase approximation, which gives rise to the pre-factor of the square gradient term in Eq. (1), deGennes[38,39] used the linear expansion of the single chain scattering function, the Debye function. Hence, physically, the small-k limit is defined by the values of k for which the linearized version remains a good approximation to the full Debye function. We outline the calculations we performed to determine these inequalities in Sec. S.1.3 of the supplementary material. Given that we used $N_s = 257$ and $\Delta x = 0.25$ in the simulations, each snapshot of the synthetic structure factor we generated consists of 129 values, with the 129th value corresponding to $\mathrm{k} \approx 12.5$. Therefore, we concluded that truncating the snapshots is necessary to conform with the small-k limit. For simplicity, we applied the $\mathrm{k} < 3$ limit to both time series, which corresponds to only using the first 33 k-values associated with each snapshot.

B. Applying dynamic mode decomposition

Two features of DMD that appealed to us are its simple formulation in terms of a best-fit linear model and its computational efficiency. We believe these features make it a good choice of technique to benchmark other, more complex techniques against. In addition to these features, the fact that no knowledge of governing equations or system parameters is required suggests that DMD has the potential to work well in a control system.

For both the critical and off-critical quenches, we trained and tested 50 DMD models to predict the synthetic structure factor at integer values of τ in the range $1 \leq \tau \leq 50$. The specific set of structure factors from earlier times used in the training of each of the models is given below. We implemented the training and testing of the DMD models using MATLAB code adapted from Ref. 44. The performance of DMD depends on the careful selection of several hyperparameters:[41,44] the number of snapshots, m; the (dimensionless) time between the snapshots, $\Delta\tau$; the rank of the reduced SVD, $\tilde{r}$; and the predictive horizon, τ_{ph}. Based on trial and error, we used $m = 10$, $\Delta\tau = 0.025$, $\tilde{r} = 3$, and $\tau_{\text{ph}} = 0.75$ to obtain the majority of our results. We also present results obtained using different values of τ_{ph}. We chose $\tilde{r} = 3$ since this value seemed to be the most consistent for accurately predicting the time evolution of the synthetic structure factor snapshots. To put the listed hyperparameter values into context, the DMD models were trained on ten uniformly synthetic structure factor snapshots in the range $\tau - 1 < \tau' \leq \tau - 0.750$, and the predictions they made extended beyond the last training snapshot by three times the length of the training range. For example, the model that predicted the snapshot of the synthetic structure factor at $\tau = 9$ was trained on the snapshots at $\tau = 8.025, 8.050, \ldots$, and 8.250.

To quantify how well the DMD models were able to predict the synthetic structure factor snapshots, the percentage errors associated with each prediction were calculated as a function of the wavenumber using

$$PE(k,\tau) = \frac{|\tilde{S}(\mathrm{k},\tau) - \tilde{S}_{DMD}(\mathrm{k},\tau)|}{\tilde{S}(\mathrm{k},\tau)} \times 100, \tag{35}$$

where $\tilde{S}(\mathrm{k},\tau)$ is the value of the synthetic structure factor snapshot to be predicted and $\tilde{S}_{DMD}(\mathrm{k},\tau)$ is the prediction of the corresponding DMD model. To analyze the errors, box plots describing the summary statistics of $PE(\mathrm{k},\tau)$ at different values of τ were plotted and compared.

Compared to fields such as fluid dynamics,[41,44] the synthetic structure factor snapshots used in this paper are not high-dimensional. Given the small-k limit and the size of Δx required to perform accurate and discretization-independent simulations, it is hard to generate high-dimensional synthetic structure factor snapshots using the method outlined in Sec. III A. Nevertheless, we were motivated to apply DMD because of the increased likelihood of our findings generalizing to higher-dimensional snapshots compared with simply applying linear regression. Furthermore, successfully demonstrating DMD might open the door to applying extensions of the algorithm, which could shift the focus of research toward working with experimental data and perhaps even the control of phase separation. We also note that the synthetic structure factor snapshots used in this paper are free of measurement noise, which is unlikely to be the case for experimental data.

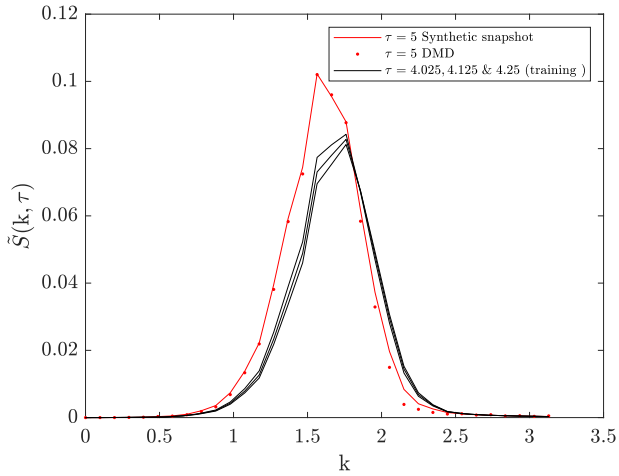

FIG. 1. Comparison between the $\tau = 5$ synthetic structure factor snapshot from the critical time series and the corresponding DMD prediction. Three of the ten snapshots on which the DMD model was trained are also shown. These snapshots correspond to $\tau = 4.025$, 4.125, and 4.250 (in order of increasing magnitude).

IV. RESULTS AND DISCUSSION

We now present our results from using DMD to model the time evolution of the synthetic structure factor snapshots from the critical and off-critical time series. Since we obtained similar results for

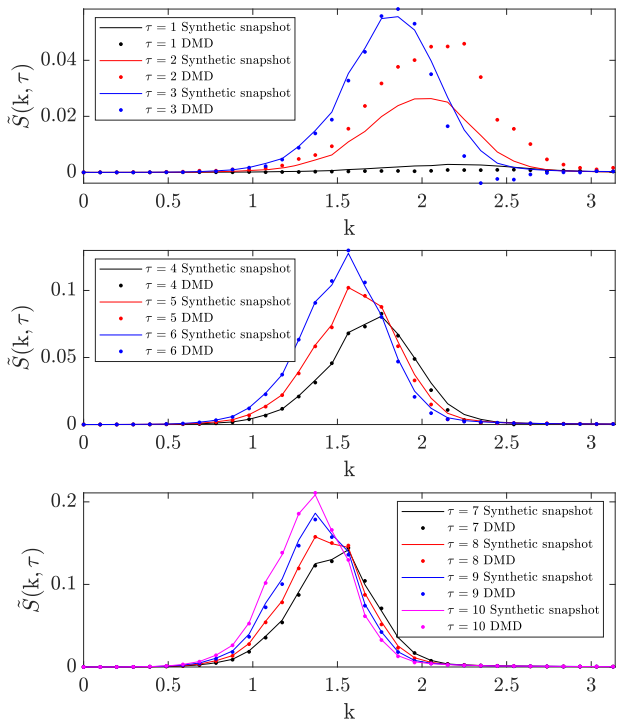

FIG. 2. Comparison between synthetic structure factor snapshots from the critical time series and those predicted by DMD models for values of τ in the range $1 \leq \tau \leq 10$. The hyperparameters used in the DMD models are listed in Sec. III B.

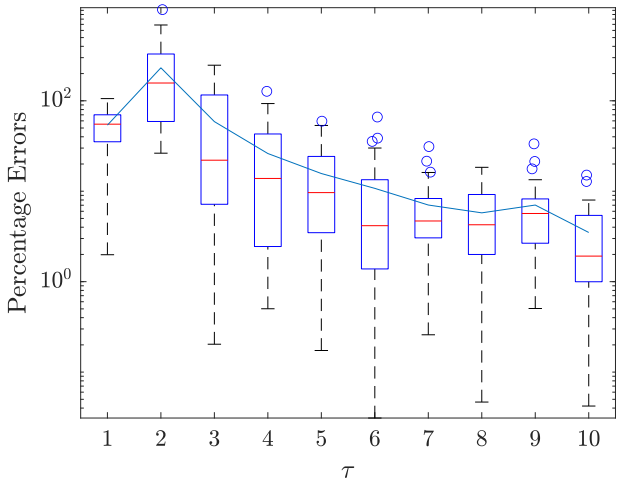

FIG. 3. Box plots of the percentage errors associated with the predictions of each DMD model in Fig. 2. In each box plot, the red line shows the median, the blue box outlines the interquartile range, the black dotted lines extend beyond the box by 1.5 times the interquartile range, and the blue circles denote outliers. The solid blue line shows the time evolution of the mean.

both, we only present the results corresponding to the critical time series in this section. The results corresponding to the off-critical time series can be found in Sec. S.2.2 of the supplementary material. To illustrate our methodology, in Fig. 1, we show one example that includes three of the ten training snapshots at $\tau = 4.025$, 4.125, and 4.250 (the other seven, at $\tau = 4$, 4.050, 4.075, 4.100, 4.150, 4.175, and 4.200, are omitted for clarity), the DMD predicted structure factor, and the synthetic structure factor at $\tau = 5$, such that the predictive horizon is $\tau_{ph} = 0.75$. Figure 1 provides qualitative justification for our choice of calculating snapshots of the structure factor every 400th time step in our simulations of spinodal decomposition such that the dimensionless time between snapshots is $\Delta\tau = 0.025$. It can be seen that the difference between structure factor snapshots is very small. Those shown correspond to the second, sixth, and tenth of ten snapshots used to train the DMD model, so we are confident that this demonstrates that taking a snapshot every 400th time step is sufficient for the purposes of demonstrating the feasibility of the DMD methodology. Further exploration of the optimum time between snapshots would benefit from engagement with experimental data, since the measurement technique will dictate the time gap between consecutive measurements of the structure factor.

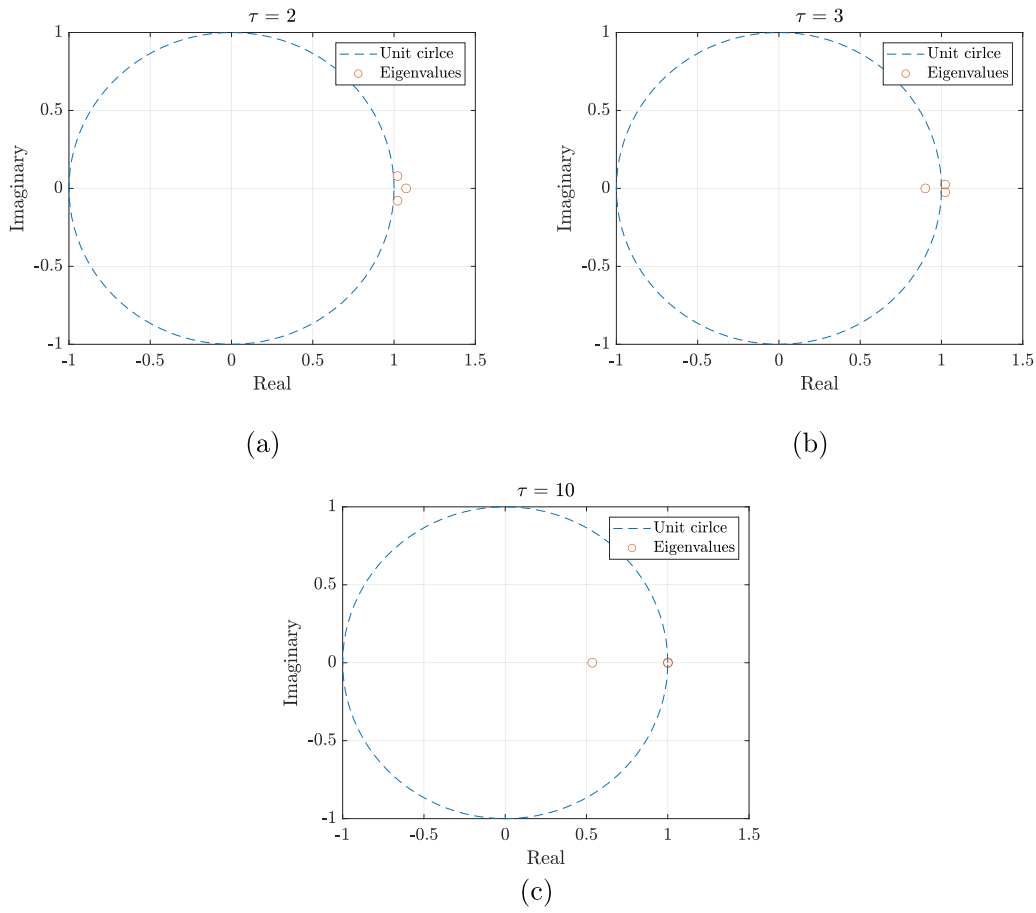

FIG. 4. Eigenvalues of the DMD models used to make the predictions of the synthetic structure factor snapshots at (a) $\tau = 2$, (b) $\tau = 3$, and (c) $\tau = 10$ in Fig. 2.

Figure 2 compares synthetic structure factor snapshots from the critical time series with those predicted by DMD models for values of τ in the range $1 \le \tau \le 10$. The hyperparameters used in the DMD models are listed in Sec. III B. We opted not to use a log scale on the y axis since this makes the curves less distinguishable. However, without a log-scale on the y axis, it is hard to see how good the predictions are at k-values where the values of the synthetic structure factor snapshots are small. Therefore, the same comparison is presented with a log-scale (base 10) on the y axis in Fig. S.3 of the supplementary material. For $\tau \le 3$, there is a low level of agreement between the synthetic structure factor snapshots and those predicted by the DMD models. The level of agreement improves for $4 \le \tau \le 10$. These observations are confirmed by Fig. 3, which shows a box plot of the percentage errors associated with the predictions of each DMD model. The solid blue line shows the time evolution of the mean percentage error, which starts off high for $\tau \le 3$ but decreases over $4 \le \tau \le 10$, eventually reaching a plateau around 3%–5%. To capture the rapid early growth of the structure factor, the eigenvalues of **A** must be highly unstable, which means the resulting DMD models are only suitable for very short-term predictions. This is exemplified in Fig. 4, which compares the eigenvalues of the DMD models used to make the predictions of the synthetic structure factor snapshots at $\tau = 2$, $\tau = 3$, and $\tau = 10$ in Fig. 2. The models corresponding to $\tau = 2$ and $\tau = 3$ have eigenvalues that extend beyond the unit circle further than those belonging to the model corresponding to $\tau = 10$. This indicates that they are more unstable. The oscillatory modes associated with the small imaginary component for the $\tau = 2$ and $\tau = 3$ eigenvalues are unphysical, further demonstrating the challenge of using DMD during the early stages.

Another comparison between synthetic structure factor snapshots from the critical time series and those predicted by DMD models is shown in Fig. 5, this time for values of τ in the range $10 \le \tau \le 50$. Again, the hyperparameters used in the DMD models are listed in Sec. III B. The same comparison is presented with a log-scale (base 10) on the y axis in Fig. S.4 of the supplementary material. For all values of τ, there is a high level of agreement between the synthetic structure factor snapshots and those predicted by the DMD models. This is confirmed by Fig. 6, which shows a box plot of the percentage errors associated with the predictions of each DMD model. The mean percentage error line is more or less flat, fluctuating between values of 1%–5%. From Figs. 2–6, we infer that, with the exception of $\tau < 3$, DMD can be used to accurately model the time evolution of the synthetic structure factor snapshots.

To investigate whether more accurate predictions of the synthetic structure factor snapshots could be made for $\tau \le 3$, we tested the predictions of several DMD models with values of $\tau_{ph} < 0.75$ at $\tau = 1$ and $\tau = 3$. Figure 7 compares the predictions of these models with the corresponding synthetic structure factor snapshots. The figure reveals that the level of agreement between the synthetic structure factor snapshots and those predicted by the DMD models increases as the value of τ_{ph} decreases. A greater reduction in the value of τ_{ph} is required at $\tau = 1$ than at $\tau = 3$ to achieve this effect. These findings suggest that there is a trade-off between the accuracy and extrapolation of the DMD predictions. Furthermore, the trade-off seems to be coupled to the value of τ for which a prediction is made: to make accurate predictions at smaller values of τ, one is constrained by having to use a smaller value of τ_{ph}.

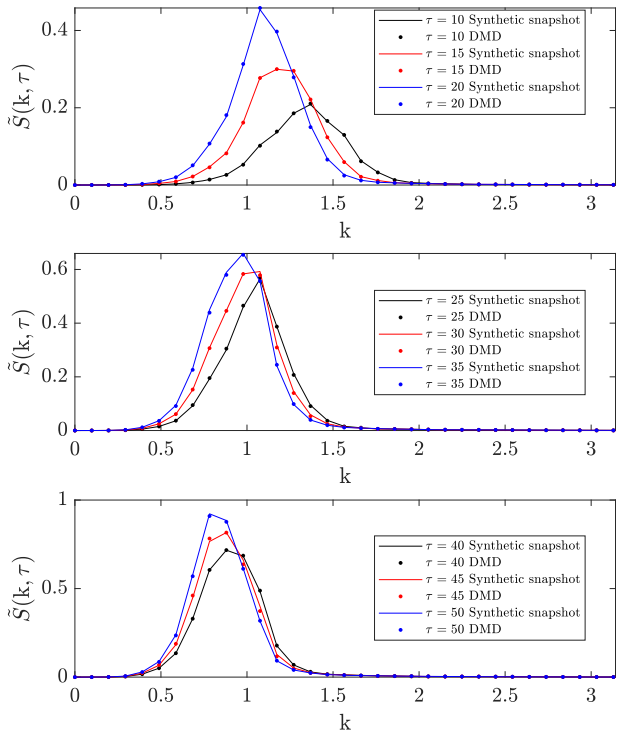

FIG. 5. Comparison between synthetic structure factor snapshots from the critical time series and those predicted by DMD models for values of τ in the range $10 \le \tau \le 50$. The hyperparameters used in the DMD models are listed in Sec. III B.

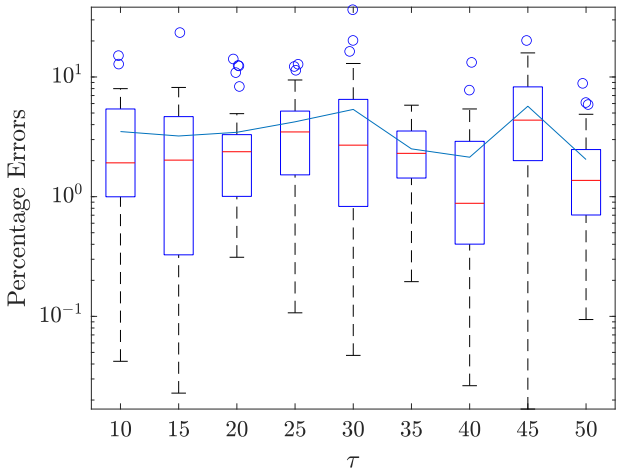

FIG. 6. Box plots of the percentage errors associated with the predictions of each DMD model in Fig. 5. In each box plot, the red line shows the median, the blue box outlines the interquartile range, the black dotted lines extend beyond the box by 1.5 times the interquartile range, and the blue circles denote outliers. The solid blue line shows the time evolution of the mean.

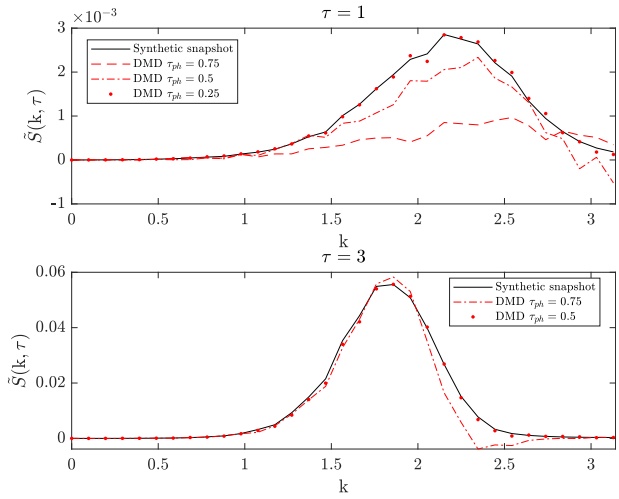

FIG. 7. Comparison between synthetic structure factor snapshots from the critical time series and those predicted by DMD models with values of $\tau_{ph} < 0.75$ at $\tau = 1$ (top panel) and $\tau = 3$ (bottom panel). The values of the other hyperparameters used in the DMD models are the same as those listed in Sec. III B.

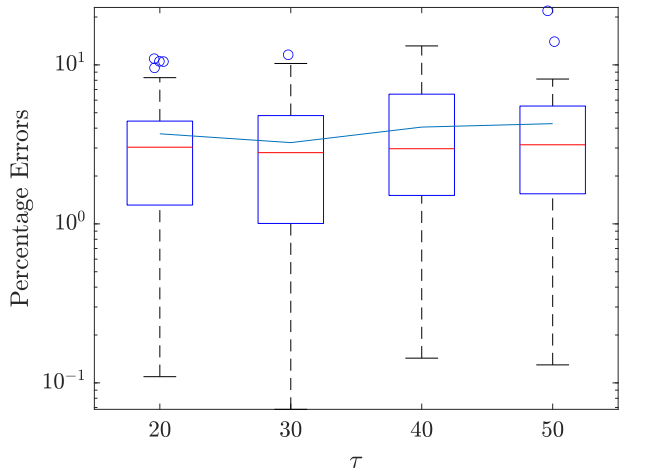

FIG. 9. Box plots of the percentage errors associated with the predictions of each DMD model in Fig. 8. In each box plot, the red line shows the median, the blue box outlines the interquartile range, the black dotted lines extend beyond the box by 1.5 times the interquartile range, and the blue circles denote outliers. The solid blue line shows the time evolution of the mean.

To test whether the trade-off between the accuracy and extrapolation of the DMD predictions is indeed time-dependent, and to explore how far into the future we are able to extrapolate with DMD, we tested the predictions of DMD models with values of $\tau_{ph} > 0.75$ at $\tau = 20, 30, 40$, and 50. We used increasingly large values of τ_{ph} to predict the synthetic structure factor snapshots corresponding to increasingly large values of τ. For these results, we used synthetic structure factor snapshots in the range $\tau - (\tau_{ph} + 0.25) < \tau' \leq \tau - \tau_{ph}$ to train the DMD models. Figure 8 compares the predictions of these models with the corresponding synthetic structure factor snapshots. The figure reveals that there is a high level of agreement between the synthetic structure factor snapshots and those predicted by the DMD models. This is confirmed by Fig. 9, which shows a box plot of the percentage errors associated with the predictions of each DMD model. The percentage errors in Fig. 9 are comparable with those in Fig. 6. The results in Figs. 8 and 9 verify that the trade-off between the accuracy and extrapolation is time dependent. Specifically, the trade-off is more important early on and becomes less important as τ increases. In other words, as τ increases, one can maintain a certain level of accuracy while predicting further into the future.

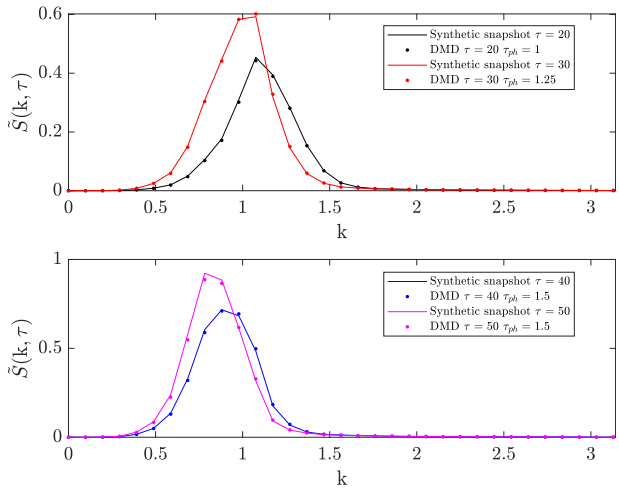

FIG. 8. Comparison between synthetic structure factor snapshots from the critical time series and those predicted by DMD models with values of $\tau_{ph} > 0.75$ at $\tau = 20$ and 30 (top panel) and $\tau = 40$ and 50 (bottom panel). The values of the other hyperparameters used in the DMD models are the same as those listed in Sec. III B.

The time-dependent accuracy-extrapolation trade-off can be linked to the growth rate of the structure factor during spinodal decomposition, which is a diffusion-like process. Early on in the process, the growth rate of the structure factor is rapid (indeed, it is exponential for a short period at the start). As time goes on, the growth rate decreases. As mentioned in Sec. III B, DMD models with $\tilde{r} = 3$ seemed to be the most consistent at accurately predicting the time evolution of the synthetic structure factor snapshots. We believe that the DMD models with $\tilde{r} < 3$ often did not capture enough of the dynamics, while models with $\tilde{r} > 3$ had an increased likelihood of containing unstable eigenvalues.

The practicality of DMD in an experimental setting depends on how the dimensionless time used to demonstrate the technique scales to physical time. Using Eqs. (6) and (30b), one can estimate a range of values of the mutual diffusion coefficient, D, for which the technique is likely to work well. Using Eq. (30b), it can be seen that for one dimensionless time unit to correspond to more than 1 s, $M < v_0\sigma^2/2k_BT(\chi - \chi_s)^2$. Substituting this inequality into Eq. (6), one obtains $|D| < \sigma^2/(\chi - \chi_s)$. In the case of the critical time series, $\sigma = 20^{\frac{1}{2}} v_0^{\frac{1}{3}}$ and $(\chi - \chi_s) \approx 2 \times 10^{-5}$. A typical value[2,30] of v_0 is 10^{-28} m^3. Substituting these values of σ, $(\chi - \chi_s)$, and v_0 into the inequality for $|D|$ yields $|D| < 10^{-13}$ m^{2}s^{-1}, which provides

an upper limit on the diffusion coefficient. If the actual diffusion coefficient is smaller than this, we would expect DMD to be able to forecast sufficiently far into the future to be of practical benefit from a control perspective. Using the representative data in Ref. 2, we calculate a typical experimental value of the diffusion coefficient: $|D_{\text{exp}}| \approx 10^{-16}$ m^{2}s^{-1}, which is three orders of magnitude lower than the estimated upper limit, which is an encouraging sign.

From the results mentioned earlier, we believe that DMD is a promising tool to enable automated control processes, particularly if combined with a method that enables microstructure characteristics to be extracted from the structure factor. We recently showed[37] that it is possible to obtain, using Gaussian Process regression, information about the phase separated structure beyond that of the length scale. Such information, specifically the interfacial area between and the interconnectivity of phase-separated regions, is critical for the properties of the final material. For example, phase separation is used to create filtration membranes, with the interfacial area and the interconnectivity of the phases determining the performance of the membrane.[53] DMD, which lends itself to real-time usage due to its low computational cost, combined with Gaussian Process regression, would enable real-time predictions of the structure factor and microstructure characteristics during spinodal decomposition to facilitate real-time adjustments of, for example, the processing temperature based on the ultimate microstructure requirements. This opens the door to the automated control of phase separation as a means of tailoring and tuning the microstructures of materials derived from polymer blends.

V. CONCLUSIONS AND FUTURE WORK

Using DMD models constructed from batches of synthetic structure factor snapshots from the critical and off-critical time series, we modeled the time evolution of the structure factor in two simulated polymer blends undergoing spinodal decomposition. Apart from early on in the process ($\tau < 3$), the DMD models were able to make accurate future predictions of the synthetic structure factor snapshots that extended beyond the last training snapshot by three times the length of the training range. We identified a trade-off between the accuracy and extrapolation of the DMD predictions. The trade-off was coupled to the value of τ for which the prediction was made, i.e., the trade-off was more important early on, decreasing in importance as τ increased. Using smaller values of τ_{ph} to make predictions of the synthetic structure factor snapshots at $\tau = 1$ and $\tau = 3$, we showed that one could improve the accuracy of the predictions at these times. We also showed that one could maintain the accuracy of predictions made at later times, specifically at $\tau = 20$, 30, 40, and 50, while increasing the value of τ_{ph}. We sought to explain the accuracy-extrapolation trade-off by making a connection with the diffusion-like nature of spinodal decomposition and the eigenvalues required by the DMD models to capture the dynamics of the synthetic structure factor snapshots. The practicality of DMD in an experimental setting will likely depend on the mutual diffusion coefficient of the blend in question.

We believe our results are promising for the development of an experimental technique to predict structure factor snapshots and microstructure characteristics corresponding to materials derived from the phase separation of polymer blends in real time. Such predictions could be useful in a control system. Of course, this will hinge on being able to replicate our results using experimental data. To address this, a logical next step should be to demonstrate whether our findings can be replicated with synthetic structure factor snapshots, which, for example, could be corrupted with external noise, have missing values, or be sampled irregularly. An extension to DMD for dealing with noise,[54] BOP-DMD, also offers the ability to quantify the uncertainty in the predictions, which could make DMD more practical to use in an experimental setting. From an automated control perspective, it would also be interesting to work with data from multi-step spinodal decomposition.[55–57] Multi-step spinodal decomposition would mimic a process in which the temperature is changed by a control system in response to predictions of the structure factor and microstructure characteristics. One might also consider investigating the application of DMDc to such a system, i.e., one with actuation.

SUPPLEMENTARY MATERIAL

Please refer to the supplementary material for additional information about generating time series of synthetic structure factor snapshots and supplementary material results.

AUTHOR DECLARATIONS

Conflict of Interest

The authors have no conflicts to disclose.

Author Contributions

Matthew Jones: Conceptualization (supporting); Data curation (lead); Formal analysis (lead); Investigation (lead); Methodology (equal); Software (lead); Visualization (lead); Writing – original draft (lead); Writing – review & editing (equal). **Nigel Clarke**: Conceptualization (lead); Funding acquisition (lead); Methodology (equal); Supervision (lead); Writing – review & editing (equal).

DATA AVAILABILITY

The data from which the results in this paper can be derived are openly available in ORDA at https://doi.org/10.15131/shef.data.29307131.v1.

REFERENCES

[1] S. Thomas, Y. Grohens, and P. Jyotishkumar, *Characterization of Polymer Blends: Miscibility, Morphology and Interfaces* (Wiley-Blackwell, 2014).
[2] J. T. Cabral and J. S. Higgins, "Spinodal nanostructures in polymer blends: On the validity of the Cahn-Hilliard length scale prediction," Prog. Polym. Sci. **81**, 1–21 (2018).
[3] S. L. Burg, A. Washington, D. M. Coles, A. Bianco, D. Mcloughlin, O. O. Mykhaylyk, J. Villanova, A. J. C. Dennison, C. J. Hill, P. Vukusic, S. Doak, S. J. Martin, M. Hutchings, S. R. Parnell, C. Vasilev, N. Clarke, A. J. Ryan, W. Furnass, M. Croucher, R. M. Dalgliesh, S. Prevost, R. Dattani, A. Parker, R. A. L. Jones, J. P. A. Fairclough, and A. J. Parnell, "Liquid–liquid phase separation morphologies

in ultra-white beetle scales and a synthetic equivalent," Commun. Chem. **2**, 100 (2019).
[4]C. M. Portela, A. Vidyasagar, S. Krödel, T. Weissenbach, D. W. Yee, J. R. Greer, and D. M. Kochmann, "Extreme mechanical resilience of self-assembled nanolabyrinthine materials," Proc. Natl. Acad. Sci. U. S. A. **117**, 5686–5693 (2020).
[5]G. A. Buxton and N. Clarke, "Predicting structure and property relations in polymeric photovoltaic devices," Phys. Rev. B **74**, 085207 (2006).
[6]R. A. L. Jones, *Soft Condensed Matter* (Oxford University Press, 2002).
[7]G. Strobl, *The Physics of Polymers* (Springer, 2007), pp. 105–150.
[8]T. Nishi, T. T. Wang, and T. K. Kwei, "Thermally induced phase separation behavior of compatible polymer mixtures," Macromolecules **8**, 227–234 (1975).
[9]J. T. Cabral, J. S. Higgins, N. A. Yerina, and S. N. Magonov, "Topography of phase-separated critical and off-critical polymer mixtures," Macromolecules **35**, 1941–1950 (2002).
[10]S. Kumar, S. Tan, L. Zheng, and D. M. Kochmann, "Inverse-designed spinodoid metamaterials," npj Comput. Mater. **6**, 73 (2020).
[11]S. Huang, L. Bai, M. Trifkovic, X. Cheng, and C. W. Macosko, "Controlling the morphology of immiscible cocontinuous polymer blends via silica nanoparticles jammed at the interface," Macromolecules **49**, 3911–3918 (2016).
[12]A. L. Esquirol, P. Sarazin, and N. Virgilio, "Tunable porous hydrogels from cocontinuous polymer blends," Macromolecules **47**, 3068–3075 (2014).
[13]J. S. Higgins and H. C. Benoit, *Polymers and Neutron Scattering* (Oxford University Press, 1994).
[14]R. Roe, *Methods of X-Ray and Neutron Scattering in Polymer Science* (Oxford University Press, 2000).
[15]J. D. Gunton, M. San Miguel, and P. S. Sahni, *Phase Transitions and Critical Phenomena* (Academic Press, London, 1983), pp. 269–466.
[16]J. D. Gunton and M. Droz, *Introduction to the Theory of Metastable and Unstable States* (Springer-Verlag, 1983).
[17]A. Z. Akcasu and R. Klein, "A nonlinear theory of transients following step temperature changes in polymer blends," Macromolecules **26**, 1429–1441 (1993).
[18]J. W. Cahn and J. E. Hilliard, "Free energy of a nonuniform system. I. Interfacial free energy," J. Chem. Phys. **28**, 258–267 (1958).
[19]J. W. Cahn, "On spinodal decomposition," Acta Metall. **9**, 795–801 (1961).
[20]H. E. Cook, "Brownian motion in spinodal decomposition," Acta Metall. **18**, 297–306 (1970).
[21]P. J. Flory, *Principles of Polymer Chemsitry* (Cornell University Press, 1953).
[22]M. L. Huggins, "Some properties of solutions of long-chain compounds," J. Phys. Chem. **46**, 151 (1942).
[23]P. G. de Gennes, "Dynamics of fluctuations and spinodal decomposition in polymer blends," J. Chem. Phys. **72**, 4756–4763 (1980).
[24]K. Binder, "Collective diffusion, nucleation, and spinodal decomposition in polymer mixtures," J. Chem. Phys. **79**, 6387–6409 (1983).
[25]H. L. Snyder, P. Meakin, and S. Reich, "Dynamical aspects of phase separation in polymer blends," Macromolecules **16**, 757–762 (1983).
[26]T. Hashimoto, J. Kumaki, and H. Kawai, "Time-resolved light scattering studies on kinetics of phase separation and phase dissolution of polymer blends. 1. Kinetics of phase separation of a binary mixture of polystyrene and poly(vinyl methyl ether)," Macromolecules **16**, 641–648 (1983).
[27]J. S. Higgins and J. T. Cabral, "A thorny problem? Spinodal decomposition in polymer blends," Macromolecules **53**, 4137–4140 (2020).
[28]J. Kumaki and T. Hashimoto, "Time-resolved light scattering studies on kinetics of phase separation and phase dissolution of polymer blends. 4. Kinetics of phase dissolution of a binary mixture of polystyrene and poly(vinyl methyl ether)," Macromolecules **19**, 763–768 (1986).
[29]K. Binder and P. Fratzl, *Phase Transformations in Materials* (Wiley, 2001), pp. 409–480.
[30]A. Z. Akcasu, I. Bahar, B. Erman, Y. Feng, and C. C. Han, "Theoretical and experimental study of dissolution of inhomogeneities formed during spinodal decomposition in polymer mixtures," J. Chem. Phys. **97**, 5782–5793 (1992).
[31]A. Z. Akcasu, B. Erman, and I. Bahar, "Nonlinear kinetics of spinodal decomposition, and dissolution of inhomogeneities formed by spinodal decomposition in polymer blends," Makromol. Chem. Macromol. Symp. **62**, 43–60 (1992).
[32]J. W. Cahn, "Phase separation by spinodal decomposition in isotropic systems," J. Chem. Phys. **42**, 93–99 (1965).
[33]J. W. Cahn, "The 1967 institute of metals lecture—Spinodal decomposition," in *The Selected Works of John W. Cahn*, edited by W. C. Carter and W. C. Johnson (The Mineral, Metals and Materials Society, 1998), pp. 166–180.
[34]N. Goldenfeld, *Lectures on Phase Transitions and the Renormalization Group* (CRC Press, 2018).
[35]R. Zwanzig, *Nonequilibrium Statistical Mechanics* (Oxford University Press, 2001).
[36]S. C. Glotzer, "Computer simulations of spinodal decomposition in polymer blends," in *Annual Reviews of Computational Physics II* (World Scientific, 1995), pp. 1–46.
[37]M. Jones and N. Clarke, "Machine learning real space microstructure characteristics from scattering data," Soft Matter **17**, 9689–9696 (2021).
[38]G. R. Strobl, "Structure evolution during spinodal decomposition of polymer blends," Macromolecules **18**, 558–563 (1985).
[39]P. G. de Gennes, *Scaling Concepts in Polymer Physics* (Cornell University Press, 1979).
[40]J. S. Langer, M. Bar-On, and H. D. Miller, "New computational method in the theory of spinodal decomposition," Phys. Rev. A **11**, 1417–1429 (1975).
[41]S. L. Brunton and J. N. Kutz, *Data-Driven Science and Engineering: Machine Learning, Dynamical Systems, and Control* (Cambridge University Press, 2019).
[42]P. J. Schmid, "Dynamic mode decomposition of numerical and experimental data," J. Fluid Mech. **656**, 5–28 (2010).
[43]J. H. Tu, C. W. Rowley, D. M. Luchtenburg, S. L. Brunton, and J. Nathan Kutz, "On dynamic mode decomposition: Theory and applications," J. Comput. Dyn. **1**, 391–421 (2014).
[44]S. L. Brunton, J. N. Kutz, J. L. Proctor, and B. W. Brunton, *Dynamic Mode Decomposition: Data-Driven Modeling of Complex Systems* (SIAM, 2016).
[45]N. Demo, M. Tezzele, and G. Rozza, "PyDMD: Python dynamic mode decomposition," J. Open Source Software **3**, 530 (2018).
[46]R. Penrose, "A generalized inverse for matrices," Math. Proc. Cambridge Philos. Soc. **51**, 406–413 (1955).
[47]A. Chakrabarti, R. Toral, J. D. Gunton, and M. Muthukumar, "Spinodal decomposition in polymer mixtures," Phys. Rev. Lett. **63**, 2072–2075 (1989).
[48]A. Chakrabarti, R. Toral, J. D. Gunton, and M. Muthukumar, "Dynamics of phase separation in a binary polymer blend of critical composition," J. Chem. Phys. **92**, 6899–6909 (1990).
[49]J. D. Gunton, R. Toral, and A. Chakrabarti, "Numerical studies of phase separation in models of binary alloys and polymer blends," Phys. Scr. **1990**(T33), 12–19.
[50]P. J. Flory, *Statistical Mechanics of Chain Molecules* (Interscience, 1969).
[51]J. Bezanson, A. Edelman, S. Karpinski, and V. B. Shah, "Julia: A fresh approach to numerical computing," SIAM Rev. **59**, 65–98 (2017).
[52]T. Besard, C. Foket, and B. De Sutter, "Effective extensible programming: Unleashing Julia on GPUs," IEEE Trans. Parallel Distrib. Syst. **30**, 827 (2019).
[53]G. R. Guillen, Y. Pan, M. Li, and E. M. V. Hoek, "Preparation and characterization of membranes formed by nonsolvent induced phase separation: A review," Ind. Eng. Chem. Res. **50**, 3798–3817 (2011).
[54]D. Sashidhar and J. N. Kutz, "Bagging, optimized dynamic mode decomposition for robust, stable forecasting with spatial and temporal uncertainty quantification," Philos. Trans. R. Soc., A **380**, 20210199 (2022); arXiv:2107.10878.
[55]N. Clarke, "Target morphologies via a two-step dissolution-quench process in polymer blends," Phys. Rev. Lett. **89**, 215506 (2002).
[56]I. C. Henderson and N. Clarke, "Two-step phase separation in polymer blends," Macromolecules **37**, 1952–1959 (2004).
[57]T. L. Tran, P. K. Chan, and D. Rousseau, "Morphology control in symmetric polymer blends using two-step phase separation," Comput. Mater. Sci. **37**, 328–335 (2006).